



Highly efficient NiMo/SiO₂-Al₂O₃ hydrodesulfurization catalyst prepared from gemini surfactant-dispersed Mo precursor

Jundong Xu, Tingting Huang, Yu Fan*

State Key Laboratory of Heavy Oil Processing, China University of Petroleum, Beijing 102249, PR China



ARTICLE INFO

Article history:

Received 23 July 2016

Received in revised form

29 September 2016

Accepted 28 October 2016

Available online 29 October 2016

Keywords:

Gemini surfactant

NiMo/SiO₂-Al₂O₃

Hydrodesulfurization catalyst

Ni-Mo-S phase

Morphology

ABSTRACT

This article proposes a novel gemini surfactant-assisted synthesis of Mo precursor for preparing NiMo/SiO₂-Al₂O₃ ultra-deep hydrodesulfurization (HDS) catalysts. The proposed method transforms polymolybdate anions into gemini surfactant-linked Mo precursor (GSMP), which facilitates the formation of highly dispersed MoS₂ phases with improved stacking and therefore produces a large number of accessible Ni-Mo-S phases after Ni incorporation. The GSMP-based NiMo/SiO₂-Al₂O₃ catalyst presents higher catalytic activity for the HDS of 4,6-dimethylbenzothiophene and fluid catalytic cracking (FCC) diesel than its counterparts prepared via impregnation and the cetyltrimethylammonium bromide-assisted hydrothermal method.

© 2016 Elsevier B.V. All rights reserved.

1. Introduction

Increasingly stringent environmental regulations and fuel standards impel refineries to produce clean diesel with ultra-low sulfur [1]. However, the presence of sterically hindered 4,6-dimethylbenzothiophene (4,6-DMDBT) makes sulfur removal from diesel a critical challenge [2]. Hydrodesulfurization (HDS) is an important technique for diesel desulfurization [3]. The key to improving HDS performance lies in the fabrication of highly active catalysts.

Mo(W)-based sulfides as active components and Ni(Co) as promoters supported on alumina have been used as HDS catalysts for more than 80 years [4]. Extensive studies indicate that there are two Co(Ni)-Mo(W)-S phases in γ -Al₂O₃-supported Co(Ni)-Mo(W) sulfides [5–9]. The type I phase with poor sulfidation has strong Mo-O-Al linkages with γ -Al₂O₃ and presents poor HDS activity, whereas the type II phase with full sulfidation possesses weak van der Waals interactions with γ -Al₂O₃ and exhibits high HDS activity. Therefore, the key point for improving the HDS activity of Mo-based sulfides lies in increasing the amount of the type II phase. The strong metal-support interaction leads to excellent dispersion but poor sulfidation of Mo oxidic species, while the weak metal-support interaction brings about superior sulfidation but poor dispersion

of Mo oxidic species [10]. In conventional alumina-supported Mo-based catalysts, the strong Mo-support interaction results from the interaction between the Mo oxides and the basic hydroxyls of γ -Al₂O₃ [11–13]. The strong interaction can be reduced using mesoporous materials, such as SBA-15 [14,15], KIT-6 [16] and MCM-41 [17,18], but their poorer mechanical strength, thermal and hydrothermal stability restrict the industrial application of these materials. The surface modification of alumina is an efficient way to weaken the metal-support interaction. Felipe Sánchez-Minero et al. [19–21] showed that modifying the alumina surface with SiO₂ reduced the number of reactive hydroxyls on the γ -Al₂O₃ surface and therefore weakened the Mo- γ -Al₂O₃ interaction, promoting the sulfidation of supported Mo oxides. However, the weakened interaction produced the metal species with large particles, decreasing the number of active metal sites.

Several methods have been developed to obtain highly dispersed metal phases, such as equilibrium deposition filtration [22,23], deposition-precipitation [24], and the chemical vapor deposition and sonochemical method [25]. These methods enhance the dispersion of metal phases but decrease the stacking of active metal phases with strong metal-support interactions, blocking the adsorption and subsequent reaction of sterically hindered 4,6-DMDBT. To improve the stacking of active metal phases, chelated metal precursors were synthesized, such as Mo₄(Hcitrate)₂O₁₁⁴⁻ complexes [26], (CoL)₂[Mo₄(C₆H₅O₇)₂O₁₁]_xH₂O complexes [27] and (NH₄)₄[Ni(OH)₆Mo₆O₁₈] [28]. However, the low stability of these complexes leads to their decomposition during the load-

* Corresponding author.

E-mail address: fanyu@cup.edu.cn (Y. Fan).

ing process and to an uneven distribution of active metal phases, reducing the activity of the corresponding catalysts. It is still a challenge for balancing the dispersion and stacking of supported metal phases to efficiently remove sterically hindered sulfur-containing compounds.

Herein, we prepare a novel NiMo/SiO₂-Al₂O₃ catalyst with the improved stacking and good dispersion of supported active phases via gemini surfactant-assisted synthesis. In this method, poly-molybdate anions were transformed into gemini surfactant-linked Mo precursor (GSMP), dispersing Mo species well and weakening the strong Mo-support interaction. Meanwhile, a hydrothermal system was adopted to decrease the viscosity of solution and increase mass transfer for improving the dispersion of Mo precursor [29]. The above measures ensured the superior dispersion of the supported Mo species with improved stacking and thereby yielded highly efficient NiMo/SiO₂-Al₂O₃ catalyst for 4,6-DMDBT HDS.

2. Experimental

2.1. Synthesis of Mo precursors

Gemini-type quaternary ammonium surfactant (C₁₆H₃₃-N(CH₃)₂-C₆H₁₂-N(CH₃)₂-C₁₆H₃₃)Br₂ (abbreviated as 16-N₂-16Br₂) was synthesized according to the literatures [30,31]. The reaction of N,N,N',N'-tetramethyl-1,6-hexanediamine ((CH₃)₂N-(CH₂)₆-N(CH₃)₂, 99 wt.%, J & K Scientific Ltd., Beijing) with 1-bromohexadecane (C₁₆H₃₃Br, 98 wt.%, J & K Scientific Ltd., Beijing) in isopropanol ((CH₃)₂CHOH, 99 wt.%, J & K Scientific Ltd., Beijing) under reflux at 85 °C for 48 h yielded the gemini surfactant 16-N₂-16Br₂, which was recrystallized from a mixture of acetone and ethanol. The products were detected by ¹H NMR in a CDCl₃ solution using a Bruker Avance apparatus (300 MHz).

A typical procedure for the synthesis of Mo-based precursor involved the following steps: firstly, 1.04 g of ammonium heptamolybdate tetrahydrate (AHT, (NH₄)₆Mo₇O₂₄·4H₂O, 99.99 wt.%, J & K Scientific Ltd., Beijing) was dissolved in 50 mL deionized water, and a hydrochloric acid solution (containing 37% HCl) was added to the aqueous solution until the pH reached 3.0. Then, at 50 °C, 20 mL of 0.074 M 16-N₂-16Br₂ solution was added to the above aqueous solution under vigorous stirring. The as-prepared mixture was acidulated to pH=3.0 by adding hydrochloric acid solution and was then stirred for 2 h at 50 °C. Finally, the suspension was washed with deionized water, centrifuged, and dried at 100 °C for 6 h. The obtained product was considered gemini surfactant-linked Mo precursor (GSMP).

2.2. Preparation of catalysts

The SiO₂-Al₂O₃ support (Shandong Alumina Plant, P.R. China) contained 96.4 wt.% Al₂O₃ and 3.6 wt.% SiO₂, with a surface area of 316 m² g⁻¹, average diameter of 8.0 nm, and pore volume of 0.63 mL g⁻¹. The support was denoted by SA.

Three MoO₃/SA catalysts, designated as Mo-GSHD, Mo-CTHD and Mo-IM, were prepared by the gemini surfactant-assisted hydrothermal deposition (GSHD), the CTAB-assisted hydrothermal deposition (CTHD) and impregnation (IM).

The preparation of oxidic Mo-GSHD involved the following steps: 4.0 g of the above SA particles (20–40 meshes) was placed in a 100 mL autoclave containing 70 mL of GSMP suspension, and the autoclave was heated at 120 °C for 24 h under rotation. Next, the obtained GSMP/SA composite was filtered, and washed with deionized water. Last, the composite was dried at 120 °C for 2 h, and calcined at 500 °C for 4 h in N₂ atmosphere. As a result, the oxidic Mo-GSHD catalyst was obtained.

For comparison, oxidic Mo-CTHD was prepared as follows: first, a (NH₄)₆Mo₇O₂₄·4H₂O aqueous solution was acidulated to pH = 3.0, and CTAB was added to obtain a suspension. Then, 4.0 g of the above SA particles (20–40 meshes) was added to a 100 mL autoclave containing 70 mL of the as-prepared suspension, and the autoclave was heated at 120 °C for 24 h under rotation; finally, the resulting composite was treated with the same procedures as those for the GSMP/SA composite. As a result, the oxidic Mo-CTHD catalyst was obtained.

Oxidic Mo-IM was prepared via impregnating 20–40 meshes SA particles with a (NH₄)₆Mo₇O₂₄·4H₂O aqueous solution. Following the impregnation, the sample was dried and calcined with the same procedures as those for the GSMP/SA composite.

The MoO₃ loadings of the Mo-IM, Mo-CTHD and Mo-GSHD catalysts, detected by X-ray fluorescence spectroscopy (XRF) on an AxiosmAX instrument, were 16.7, 17.0 and 16.8 wt.%, respectively.

The loading of NiO on the three MoO₃/SA catalysts was carried out by impregnating Mo-GSHD, Mo-CTHD and Mo-IM with nickel nitrate (Ni(NO₃)₂·6H₂O, 98 wt.%) as the Ni precursor. After impregnation, the products were dried at 120 °C for 2 h and calcined at 500 °C for 4 h in N₂ to produce three oxidic NiMo/SA catalysts, denoted as NiMo-GSHD, NiMo-CTHD and NiMo-IM. According to the XRF results, the contents of MoO₃ in NiMo-IM, NiMo-CTHD and NiMo-GSHD were 16.3, 16.7 and 16.5 wt.%, respectively; the contents of NiO in NiMo-IM, NiMo-CTHD and NiMo-GSHD were 3.8, 3.5 and 3.6 wt.%, respectively.

2.3. Characterizations

Fourier transform infrared (FT-IR) experiments were measured on a Nicolet 6700 FT-IR spectrometer, and the spectra of samples were recorded in the wavenumber range of 650–4000 cm⁻¹ at a 4 cm⁻¹ resolution.

NO adsorption followed by FT-IR spectroscopy (Nicolet 6700 FT-IR spectrometer) was conducted using self-supported wafers (5–10 mg/cm²) of the oxidic catalysts that were mounted in the FT-IR cell. The catalyst was sulfided in situ at 360 °C for 2 h in a flow of 15% H₂S/H₂ and then flushed with He at 360 °C for 1 h. After cooling to room temperature in a pure He flow, the cell was evacuated to 10⁻³ Pa. The sample was exposed to 6650 Pa of NO for 30 min, followed by flushing the gas phase NO with pure He, and subsequently the spectra were recorded. The background was subtracted in all reported spectra.

Laser Raman (LR) experiments were performed on a Bruker Raman spectrometer, and the spectra were recorded in 3600–100 cm⁻¹, using the Nd-YAG laser excited at 532 nm as the laser source. Elemental analyses were acquired through inductively coupled plasma-optical emission spectrometry (ICP-OES) on a Perkin Elmer instrument combined with 2400 II CHN element analyzer.

N₂ adsorption-desorption experiments of the support SA and catalysts were conducted on a Micromeritics ASAP 2420 instrument. The samples were pretreated at 250 °C under a vacuum of 10⁻³ Pa for 15 h prior to the experiments, and subsequently transferred to the analysis station for adsorption-desorption at -196 °C.

X-ray diffraction (XRD) analyses were conducted on a Bruker D8 Advance instrument (40 kV and 30 mA), using Cu K α radiation ($\lambda = 1.54 \text{ \AA}$). The scanning range of 2 θ was between 10 and 80° with a speed at 4°/min.

The hydrogen temperature-programmed reduction (H₂-TPR) experiments of the oxidic catalysts were carried out with a self-established device. First, 100 mg of each sample were heated at 450 °C for 2 h in an Ar atmosphere and subsequently the sample was cooled down to 60 °C. Subsequently, the sample was heated from 60 to 1050 °C with a rate of 10 °C/min and kept at 1050 °C for

30 min in a 10% H₂/N₂ flow. The H₂ consumption for reducing the oxidic metal in sample was determined via a TCD detector.

UV-vis diffuse reflectance spectroscopy (DRS) was conducted on a UV-vis spectrophotometer (Hitachi U-4100) employing an integration sphere diffuse reflectance attachment. The powder samples were introduced into a quartz cell and the spectra were recorded in 200–800 nm with the SA support used as the baseline. The band gap energy (E_g) for allowed transitions was employed to obtain the local structure information of the surface molybdenum oxides and it was determined according to the literature [32].

The morphologies of the active metal phases on the sulfide samples were acquired on a FEI Tecnai G2 F20 transmission electron microscope (TEM) with an accelerating voltage of 200 kV. Chemical mapping by the energy dispersive X-ray spectrometer (EDS) was measured on a Link-ISIS-300 X-ray spectrometer. High-angle annular dark-field scanning transmission electron microscopy (HAADF-STEM) of the oxidic catalysts was also carried out on the TEM instrument mentioned above. The sample powder was placed on a micro grid carbon polymer supported on a copper grid by adding a few droplets of the sample suspension in ethanol on the micro grid, and then dried under an infrared lamp.

X-ray photoelectron spectroscopy (XPS) analyses of the sulfided samples were conducted on an ESCA Lab 250 electron spectrometer (VG Scientific) equipped with an Al K α radiation with an energy resolution of 0.4 eV. The spectra were scanned at a pressure of 3×10^{-8} Pa. Before measurement, the sulfided samples were kept in cyclohexane to avoid oxidation. The sulfided sample was mounted on a holder and subsequently transferred to the XPS instrument at once. The binding energy of Al 2p peak (74.5 eV) was set as an internal standard. To determine the contents of Mo⁴⁺, Mo⁵⁺ and Mo⁶⁺ species, the spectra were fitted to a Shirley-Linear background using XPSPEAK version 4.1 software [33]. The deconvolution of the Mo 3d spectra was completed by the mixed Gaussian-Lorentzian function [34,35].

2.4. Catalyst assessment

The catalytic activities of Mo-GSHD, Mo-CTHD, and Mo-IM and the corresponding bimetallic catalysts for 4,6-DMDBT HDS were tested in a continuous-flow fixed bed microreactor with an 8.0 mm internal diameter and 300 mm length. 0.8 wt.% 4,6-DMDBT (98 wt.%, J & K Scientific Ltd., Beijing) in naphthalene (C₁₀H₁₈, 99 wt.%) was used as a model compound. Before loaded into reactor, the catalyst was crushed and sieved to 20–40 meshes and diluted with quartz granules of the same volume and size. Before the reaction, the catalyst was pre-sulfided at 360 °C for 6 h with 3 wt.% carbon disulfide in n-heptane. After sulfidation, the activity of the catalyst was assessed at temperature 330 °C, pressure 4.0 MPa, liquid hourly space velocity (LHSV) 20 h⁻¹ and H₂/model compound volumetric ratio of 400. The liquid product was collected after a steady state and analyzed using a Finnigan Trace GC-MS spectrometry with a Trace Ultra gas chromatograph equipped with an HP-5MS (60 m × 0.25 mm × 0.25 μm) capillary column.

The 4,6-DMDBT HDS was assumed as a pseudo-first order reaction, and the activity of catalyst was calculated by the following equation [36]:

$$k_{HDS} = \frac{F}{m} \ln \left(\frac{1}{1-x} \right) \quad (1)$$

where k_{HDS} is the reaction rate constant of 4,6-DMDBT HDS in mol g⁻¹ s⁻¹, F is the molar feed rate of 4,6-DMDBT in mol s⁻¹, m is the catalyst mass in grams, and x is the 4,6-DMDBT conversion.

According to the literatures [37–39], the dispersion of Mo (f_{Mo}) was calculated from Eq. (2) and turnover frequency (TOF) was calculated from Eq. (3).

$$f_{Mo} = \frac{\sum_{i=1}^t (6n_i - 6)}{\sum_{i=1}^t (3n_i^2 - 3n_i + 1)} \quad (2)$$

$$TOF = \frac{F \cdot x}{n_{Mo} \cdot f_{Mo}} \quad (3)$$

where n_i is the number of Mo atoms along one edge of a MoS₂ slab calculated by its length ($L = 3.2(2n_i - 1)\text{\AA}$), and t is the number of total slabs, F is the molar feed rate of 4,6-DMDBT in mol s⁻¹, x is the 4,6-DMDBT conversion, n_{Mo} is the amount of Mo atoms in the catalyst in mol.

In addition, the HDS performance of the sulfided NiMo/SA catalysts was assessed using FCC diesel acquired from a Chinese refinery. The physical properties of the FCC diesel (Table S1) are sulfur content at 3920 μg g⁻¹, density at 0.845 g cm⁻³, and boiling point at 212–358 °C. The HDS reaction with FCC diesel as feedstock was evaluated under the following conditions: LHSV 2.5 h⁻¹, pressure 6.0 MPa, temperature 350 °C, and H₂/oil volume ratio of 500. The liquid product was collected for analysis after a steady state. The total sulfur content of FCC diesel was measured using an Analytik Jena Multi EA 5000 (Germany) instrument via the pyrolysis method, in accordance with the international standard (ASTM D5453).

3. Results and discussion

3.1. Properties of GSMP

To explore the properties of GSMP, the following characterization results were presented. The elemental contents of GSMP determined by ICP and CHN element analyzer were Mo: 30.83 wt.%, C: 43.30 wt.%, H: 7.79 wt.%, N: 2.35 wt.%, O: 15.73 wt.%. Therefore, the chemical composition of the GSMP was calculated to be C_{3.61}H_{7.79}N_{0.17}Mo_{0.32}O_{0.98}, almost equal to (C₄₂H₉₀N₂)₂Mo₈O₂₆. The LR measurement is an efficient method to determine the aggregation of transitional metal salts. To determine the inorganic core of GSMP, the LR spectrum of GSMP is shown in Fig. 1a. According to the synthesis condition of GSMP, the inorganic core of GSMP is either Mo₇O₂₄⁶⁻ or Mo₈O₂₆⁴⁻, so the LR spectrum of AHT is also presented in Fig. 1a. AHT shows vibrational bands at 934 and 880, 860, 630, 550–308 and 220 cm⁻¹, which are attributed to the asymmetric and symmetric Mo=O terminal stretches, Mo–O–Mo asymmetric stretch, Mo–O–Mo symmetric stretch, Mo=O bending vibrations, and Mo–O–Mo deformation [40], respectively. In contrast to AHT, GSMP displays the vibrational bands at 963, 947 and 918 cm⁻¹ belonging to Mo=O terminal vibration, the bands at 856 and 766 cm⁻¹ belonging to the Mo–O–Mo asymmetric stretch, and the bands at 515 cm⁻¹ attributed to the Mo–O–Mo symmetric stretch. Besides the above distinction in the Mo=O terminal stretches (934 and 880 cm⁻¹ for AHT versus 963 and 918 cm⁻¹ for GSMP), the LR spectrum of GSMP have a band at 766 cm⁻¹, which is the characteristic peak of Mo₈O₂₆⁴⁻ anions [40] but is absent for the Mo₇O₂₄⁶⁻ anions (the inset of Fig. 1a). The above analyses demonstrate that the inorganic core of GSMP is Mo₈O₂₆⁴⁻, not Mo₇O₂₄⁶⁻. In addition, no other peaks appear in the LR spectrum of GSMP except for the Mo₈O₂₆⁴⁻ moiety. From the FT-IR spectrum of GSMP (Fig. 1b), the peak at 2952 cm⁻¹ is assigned to the stretching vibration of –CH₃, while the peaks at 2921 and 2850 cm⁻¹ are, respectively, attributed to the stretching vibrations of –CH₂– and

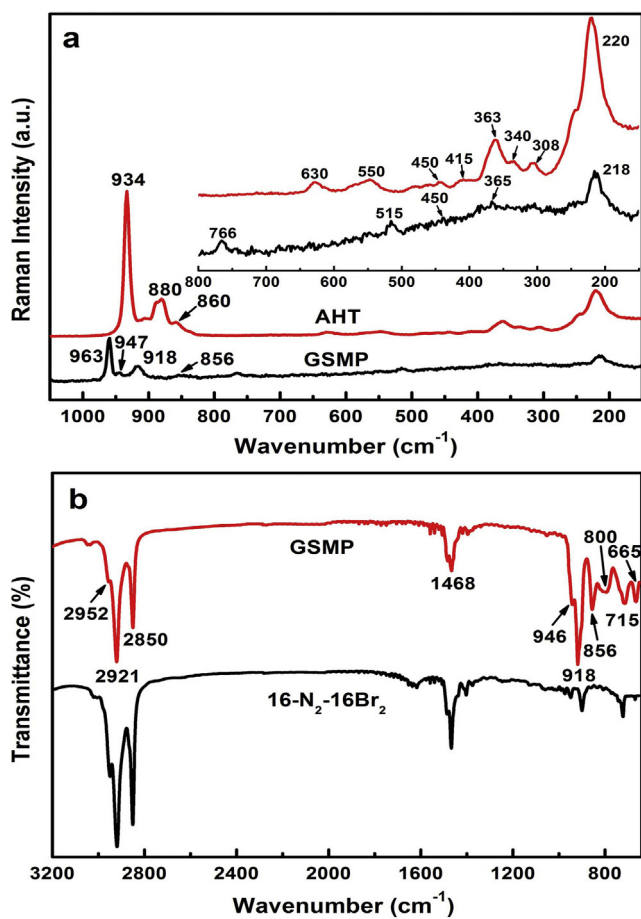


Fig. 1. LR spectra of AHT and GSMP at 1050–150 cm⁻¹, inset at 800–150 cm⁻¹ (a); FT-IR spectra of 16-N₂-16Br₂ and GSMP at 3200–650 cm⁻¹ (b).

–(CH₂)_n– (n > 4), and the peaks at 1468 and 715 cm⁻¹ are attributed, respectively, to the scissoring vibration of –CH₂– and –(CH₂)_n– (n > 4) [41]. In addition, the peaks of 650–960 cm⁻¹ are attributed to the vibrations of Mo=O and Mo–O–Mo [40]. No other peaks are seen in the FT-IR spectrum of GSMP except for the 16-N₂-16²⁺ and Mo₈O₂₆⁴⁻ moieties. The above results indicate that GSMP is a composite of Mo₈O₂₆⁴⁻ and gemini surfactant without other impurities. Moreover, GSMP has a periodic layered structure (Fig. S1).

It has been documented that cationic organoammonium interacts with polyoxomolybdate anions via the charge effect [42,43]. Herein, the strong electrostatic interaction between the 16-N₂-16²⁺ cations and polyoxomolybdate anions results in the linkage between Mo₈O₂₆⁴⁻ species and gemini surfactant. The 16-N₂-16²⁺ cations act as both the counter ions and the stabilizing agent to interact with Mo₈O₂₆⁴⁻ to form stable GSMP in aqueous solution.

3.2. Loading of GSMP onto SA

To determine the deposition of GSMP onto SA, nitrogen adsorption-desorption, FT-IR experiments were performed. The nitrogen adsorption-desorption isotherms of SA, GSMP/SA and Mo-GSHD are exhibited in Fig. 2a. The results indicate that all the isotherms are type IV, with the characteristics of mesoporous materials. Their hysteresis loops at relative pressures (P/P₀) greater than 0.43 are type H₂, indicating the presence of ink bottle pores [44]. Fig. 2b shows that the most probable pore size of GSMP/SA is smaller than SA. The results in Table 1 show that GSMP/SA has a lower specific surface area (S_g), pore volume (V_p) and average pore diameter (D_p) than SA, verifying the loading of GSMP onto SA. Mo-

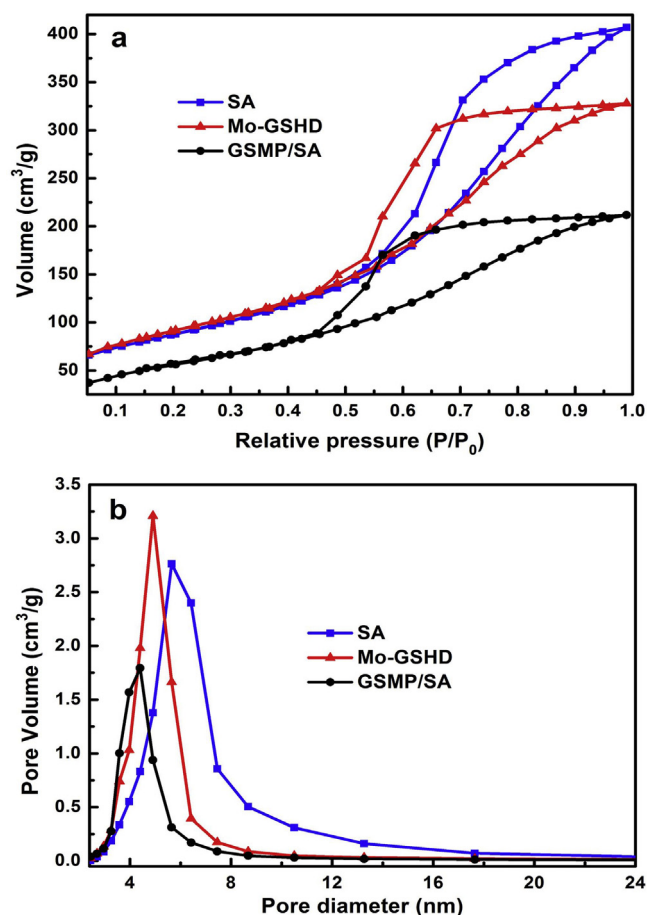


Fig. 2. N₂ adsorption-desorption isotherms (a) and BJH pore size distribution curves of SA, GSMP/SA and Mo-GSHD (b).

Table 1
Textural properties of SA, GSMP/SA, Mo-IM, Mo-CTHD and Mo-GSHD.

Sample	S _g ^a (m ² g ⁻¹)	V _p ^b (cm ³ g ⁻¹)	D _p ^c (nm)
SA	316	0.63	8.0
GSMP/SA	212	0.33	6.2
Mo-IM	269	0.44	6.5
Mo-CTHD	291	0.50	6.9
Mo-GSHD	304	0.55	7.2

^a BET specific surface area.

^b Pore volume.

^c Average pore diameter (4 V_p/S_g).

GSHD, obtained by calcining GSMP/SA, has larger S_g, D_p and V_p than GSMP/SA due to the decomposition of the organic groups of GSMP. GSMP/SA was characterized by FT-IR, and the results are shown in Fig. 3. Compared with GSMP, GSMP/SA also presents peaks at 2921, 2850 and 1468 cm⁻¹, which are ascribed to the asymmetric stretch of –CH₂– and –(CH₂)_n– (n > 4) and the scissoring vibration of –CH₂–. In addition, due to the existence of SA, the peak belonging to the stretching vibration of –CH₃ undergoes a shift from 2952 cm⁻¹ for GSMP to 2960 cm⁻¹ for GSMP/SA (inset of Fig. 3), indicating the interaction between GSMP and the SA support. The above results confirm that GSMP are supported on SA and interact with the SA support.

The loading of GSMP was carried out under hydrothermal condition. The low viscosity of the hydrothermal system facilitates the diffusion of GSMP into the pore channels of the SA support; during drying, the long alkyl chains in GSMP prevent the aggregation of molybdate; during calcination, the decomposition of the

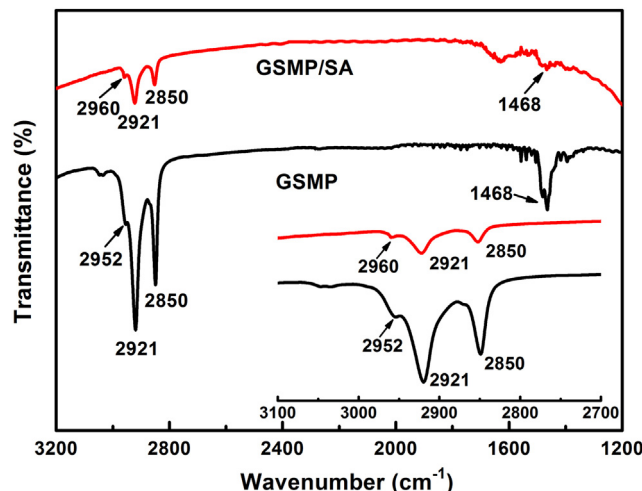


Fig. 3. FT-IR spectra of GSMP and GSMP/SA, inset at 3100–2700 cm^{-1} .

long alkyl chains in GSMP produces carbon species that make the metal oxides separate from each other. Thus, Mo species are distributed uniformly into the support, as evidenced by the following characterizations.

3.3. Characterizations of the oxidic Mo/SA and NiMo/SA catalysts

3.3.1. N_2 adsorption-desorption and XRD

Pore structure data from the N_2 adsorption-desorption experiments are presented in Table 1. Compared to the SA support, the surface areas of Mo-IM, Mo-CTHD and Mo-GSHD decrease by 14.7%, 7.6% and 3.6%, respectively; the pore volumes of Mo-IM, Mo-CTHD and Mo-GSHD decrease by 30.2%, 20.6% and 12.7%, respectively; and the average pore diameters of Mo-IM, Mo-CTHD and Mo-GSHD decrease by 18.8%, 13.8% and 10.0%, respectively. These decreases are because Mo-IM and Mo-CTHD have larger MoO_3 particles that cause partial closing of the SA pores, while Mo-GSHD has small MoO_3 particles with little influence on the catalyst pore structure [45].

The XRD patterns of the monometallic catalysts Mo-IM, Mo-CTHD and Mo-GSHD and the corresponding bimetallic catalysts NiMo-IM, NiMo-CTHD and NiMo-GSHD are shown in Fig. 4. All the samples exhibit peaks at $2\theta = 37.4^\circ$, 45.7° and 66.8° , which are assigned to the support $\gamma\text{-Al}_2\text{O}_3$ (JCPDS card no. 29-1486), while Mo-IM has additional peaks at $2\theta = 12.7^\circ$, 23.4° , 25.7° and 27.3° corresponding to bulk MoO_3 crystallites (JCPDS card no. 05-0508), and NiMo-IM has an additional peak at 27.3° . It is known that the addition of Ni improves the dispersion of oxidic Mo species [46], and thereby the XRD peak intensity of MoO_3 in the catalysts after Ni addition decreases. After Ni addition, the strongest peak intensity of MoO_3 at 27.3° obviously decreases, while the other peaks disappear with the high scanning rate ($4^\circ/\text{min}$) in the XRD pattern. These results indicate that large MoO_3 particles were formed in Mo-IM and NiMo-IM. In contrast, no bulk MoO_3 peaks are detected in the XRD patterns of Mo-CTHD, Mo-GSHD, NiMo-CTHD and NiMo-GSHD, indicating that MoO_3 is dispersed on the supports of these catalysts. The low NiO loading results in no characteristic peaks of NiO observed in the patterns of the bimetallic catalysts [47].

3.3.2. UV-vis DRS, HAADF-STEM and H_2 -TPR

To acquire more information about the existing state of the oxidic Ni and Mo species in the catalysts, UV-vis DRS, HAADF-STEM and H_2 -TPR were performed. The UV-vis DRS spectra of Mo-IM, Mo-CTHD and Mo-GSHD after subtracting the background of SA are shown in Fig. 5. The absorption band of ligand-to-metal charge

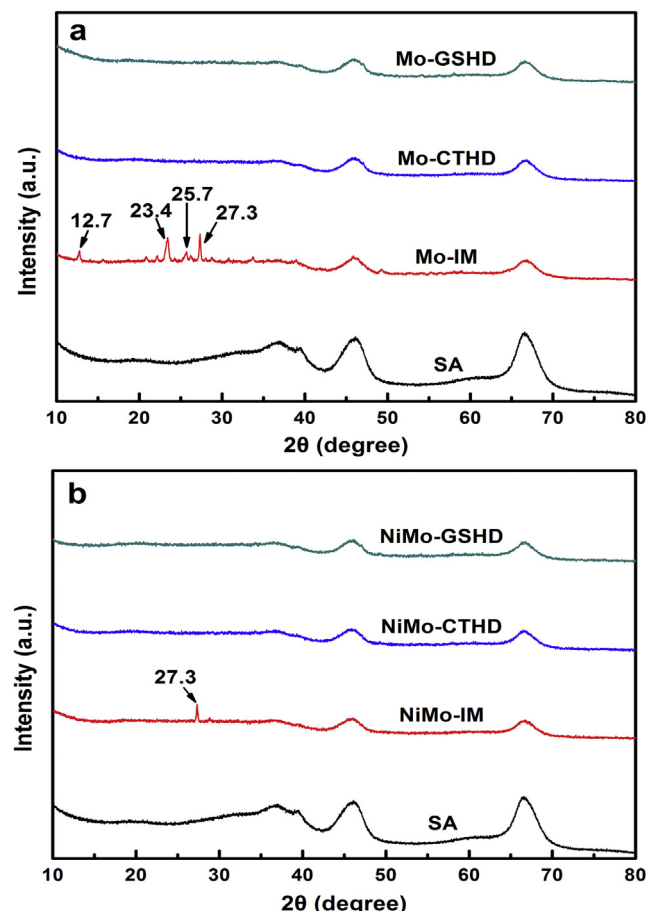


Fig. 4. XRD patterns of the support and the three monometallic catalysts (a); the support and the three bimetallic catalysts (b).

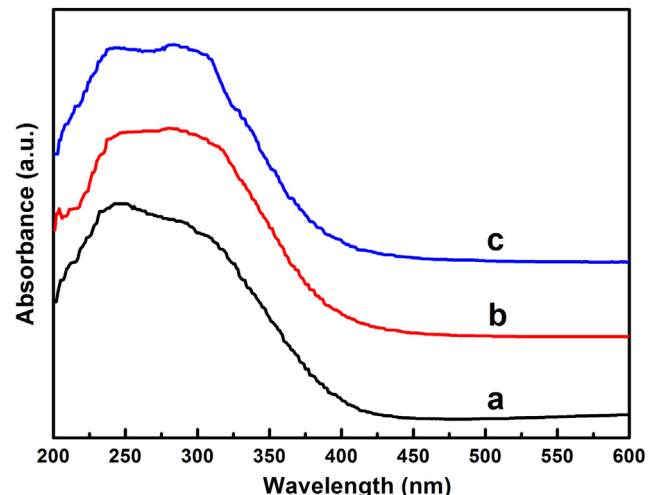


Fig. 5. UV-vis DRS spectra of oxidic Mo-IM (a), Mo-CTHD (b), Mo-GSHD (c).

transfer of $\text{O}^{2-} \rightarrow \text{Mo}^{6+}$ can be seen in 200–400 nm [14,48]. The different state of molybdenum coordination and aggregation results in distinct band position, for example, isolated (tetrahedral, T_d) molybdate species with an absorption band at 230–260 nm and polymolybdate (octahedral, O_h) species with an absorption band at 280–320 nm. All three catalysts exhibit an absorption band corresponding to the mixture of Mo^{6+} oxides in tetrahedral (T_d) and octahedral (O_h) coordination. Mo-IM presents a strong absorption

peak centered at 230–260 nm, indicating that the molybdenum species are mainly attributed to tetrahedrally coordinated Mo^{6+} (Td). In contrast, Mo-CTHD and Mo-GSHD exhibit strong absorption peaks centered at 280–320 nm, indicating that the molybdenum species are mainly attributed to octahedrally coordinated Mo^{6+} (O_h). The calculated values of the band gap energy (Eg) for Mo-IM, Mo-CTHD and Mo-GSHD are 3.1, 3.3 and 3.6 eV, respectively (Fig. S2). According to the literature [49], the band gap energy increases as the size of the metal particles decreases, indicating that Mo-GSHD possesses smaller metal particles than Mo-IM and Mo-CTHD.

The HAADF-STEM analyses combined with the EDS and element mapping of NiMo-IM, NiMo-CTHD and NiMo-GSHD were made, and the results are presented in Fig. 6. The EDS patterns of the three samples indicate that the contents of MoO_3 in NiMo-IM, NiMo-CTHD and NiMo-GSHD are 16.1, 16.4 and 16.3 wt.%, respectively, and the contents of NiO in NiMo-IM, NiMo-CTHD and NiMo-GSHD are 3.6, 3.2 and 3.3 wt.%, respectively, in agreement with the XRF results. The comparison of the Ni, Mo mapping images in NiMo-IM (Fig. 6a), NiMo-CTHD (Fig. 6b) and NiMo-GSHD (Fig. 6c) shows that NiMo-GSHD possesses smaller Ni and Mo species than the other two catalysts.

The H_2 -TPR experiment was performed to determine the metal-support interaction in the oxidic catalysts, and the results are shown in Fig. 7. From the H_2 -TPR patterns of Mo-IM, Mo-CTHD and Mo-GSHD, two reduction peaks are observed, indicating the two-step reduction of MoO_3 , i.e., $\text{MoO}_3 \rightarrow \text{MoO}_2 \rightarrow \text{Mo}$. The low-temperature peak is the reduction of $\text{Mo}^{6+} \rightarrow \text{Mo}^{4+}$ of octahedral Mo species, and the high-temperature peak is assigned to the deep reduction of all Mo species, including the further reduction of the octahedral Mo species and the partial reduction of the tetrahedral Mo species with strong metal-support interaction [50–53]. The low-temperature peaks of Mo-IM, Mo-CTHD and Mo-GSHD are 466, 448 and 445 °C, respectively, indicating that the Mo-support interactions of Mo-CTHD and Mo-GSHD are weaker than Mo-IM. The high-temperature peaks of the three monometallic catalysts are the same.

After the incorporation of Ni into Mo/SA, the TPR patterns of the corresponding catalysts also display two main peaks, and a shoulder peak is seen at 556 °C [51], which is assigned to the reduction of Ni species. Compared with the patterns of the monometallic catalysts, the TPR patterns of the corresponding bimetallic catalysts move to lower temperature, showing that Ni decreases the reduction temperature of Mo species and improves the reducibility of MoO_3 . For NiMo-GSHD, the low-temperature peak belongs to the partial reduction ($\text{Mo}^{6+} \rightarrow \text{Mo}^{4+}$) of octahedral Mo species shifts to 382 °C, a decrease of 63 °C compared to Mo-GSHD. The other two bimetallic catalysts have similar decreases of the low-temperature peak. NiMo-CTHD and NiMo-GSHD have lower temperatures for their low-temperature peaks than NiMo-IM, indicating the weaker Mo-support interaction in NiMo-CTHD and NiMo-GSHD than in NiMo-IM [50].

3.4. Characterizations of the sulfided Mo/SA and NiMo/SA catalysts

3.4.1. XPS

To attain further insight into the chemical state, surface composition, dispersion and sulfidation degree of metal species in the prepared catalysts, XPS measurements were carried out for the sulfided Mo-IM, Mo-CTHD and Mo-GSHD catalysts. According to the literatures [34,35], the decomposition of the Mo3d spectra was acquired after subtracting a continuous background of secondary electrons (Shirley method). The XPS spectra of the prepared catalysts are resolved into a main peak ($3\text{d}_{5/2}$) and a related peak ($3\text{d}_{3/2}$), and the difference of the binding energy between $3\text{d}_{3/2}$ and $3\text{d}_{5/2}$ is

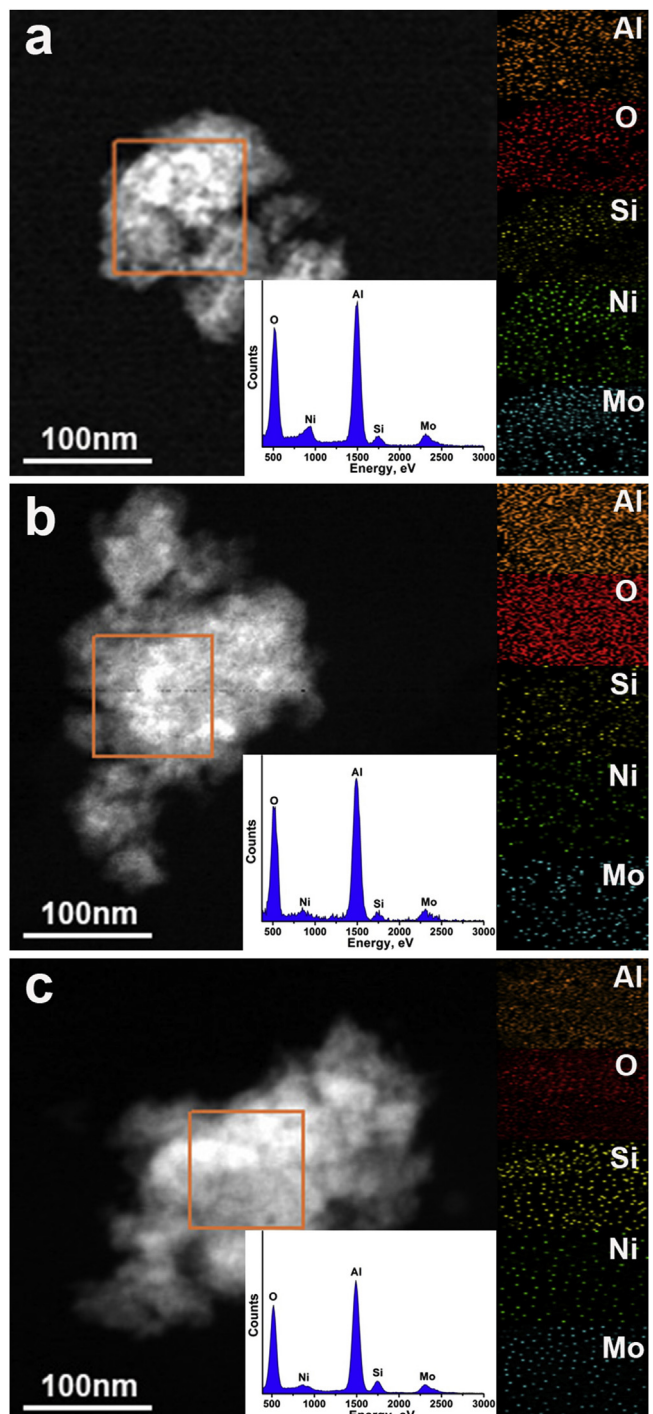


Fig. 6. HAADF-STEM results of oxidic NiMo-IM (a), NiMo-CTHD (b) and NiMo-GSHD (c). Insets display EDS patterns and the mapping images of Al (orange), O (red), Si (yellow), Ni (green), and Mo (blue) that present the element distributions for the selected regions in orange squares. (For interpretation of the references to colour in this figure legend, the reader is referred to the web version of this article.)

approximately 3.2 eV. The width ratio at half height between $3\text{d}_{3/2}$ and $3\text{d}_{5/2}$ is approximately 1.2, and the ratio of the relative area between $3\text{d}_{5/2}$ and $3\text{d}_{3/2}$ is approximately 1.5 [35].

The experimental and fitted XPS patterns of Mo3d for the three sulfided catalysts are exhibited in Fig. 8. The binding energies at 229.0 ± 0.1 eV and 232.1 ± 0.1 eV are ascribed to the $3\text{d}_{5/2}$ and $3\text{d}_{3/2}$ levels of MoS_2 (Mo^{4+}), and those at 230.2 ± 0.1 eV and 233.4 ± 0.1 eV are ascribed to the intermediate oxidation

Table 2

Fitting results of XPS on the different catalysts.

Catalyst	Mo/Al	Ni/Al	Mo _{sulfidation}	NiO _x phase	NiS _x phase	NiMoS phase
Mo-IM	0.076	–	48.1%	–	–	–
Mo-CTHD	0.093	–	55.1%	–	–	–
Mo-GSHD	0.115	–	60.7%	–	–	–
NiMo-IM	0.087	0.030	56.5%	32.8%	15.8%	51.4%
NiMo-CTHD	0.114	0.036	63.4%	28.7%	12.1%	59.2%
NiMo-GSHD	0.138	0.041	67.2%	24.7%	9.7%	65.6%

state MoO_xS_y (Mo⁵⁺). The binding energies at 232.2 ± 0.1 eV and 235.3 ± 0.1 eV are ascribed to MoO₃ (Mo⁶⁺) [35]. The spectra also contain the S2s peak at 226.0 ± 0.1 eV [54]. The sulfidation degree of molybdenum, Mo_{sulfidation}, is defined as the ratio of MoS₂ (Mo⁴⁺) to the sum of MoS₂ (Mo⁴⁺), MoO_xS_y (Mo⁵⁺) and MoO₃ (Mo⁶⁺), i.e., $\text{Mo}_{\text{sulfidation}} = \text{Mo}^{4+}/(\text{Mo}^{4+} + \text{Mo}^{5+} + \text{Mo}^{6+})$ [55]. The fitting results of the XPS spectra in Table 2 indicate that the sulfidation degrees of Mo-GSHD, Mo-CTHD and Mo-IM are 60.7% and 55.1% and 48.1%, respectively, indicating Mo-GSHD has the highest Mo sulfidation degree. Compared with Mo-IM, Mo-GSHD, which has weaker metal-support interaction (Fig. 7), has the higher Mo sulfidation. Although Mo-GSHD and Mo-CTHD possess similar strength of metal-support interaction (Fig. 7), Mo-GSHD has higher Mo sulfidation than Mo-CTHD because the former has higher Mo dispersion (Fig. 6), which exposes more Mo species to be sulfided. As shown in Table 2, combination of Ni enhances the Mo sulfidation degree of the three monometallic catalysts because Ni promotes Mo reduction, as evidenced in the H₂-TPR results.

Ni2p spectra of the three bimetallic sulfided catalysts are shown in Fig. 9. On the surface of the sulfided bimetallic catalysts, Ni species exist as NiO_x, NiS_x (Ni₉S₈, NiS and Ni₂S₃) and NiMoS [35]. The Ni2p spectra are decomposed according to the literature [35], and the relative quantities of NiO_x, NiS_x and NiMoS phases are listed in Table 2. Compared with sulfided NiMo-IM and NiMo-CTHD, sulfided NiMo-GSHD has a higher proportion (65.6%) of NiMoS phase, indicating more NiMoS phases on NiMo-GSHD.

The surface atomic ratios of Mo/Al and Ni/Al in the three bimetallic catalysts were detected by XPS, and the results are shown in Table 2. Though the three catalysts possess the same metal contents (obtained by XRF), NiMo-GSHD has a higher surface atomic ratio than the other two catalysts, indicating the better dispersion of Mo species supported on NiMo-GSHD as compared to NiMo-CTHD and NiMo-IM [55].

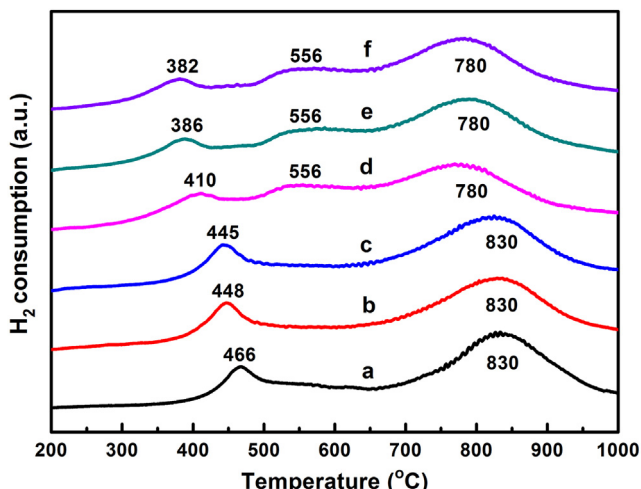


Fig. 7. H₂-TPR patterns of oxidic Mo-IM (a), Mo-CTHD (b), Mo-GSHD (c), NiMo-IM (d), NiMo-CTHD (e) and NiMo-GSHD (f).

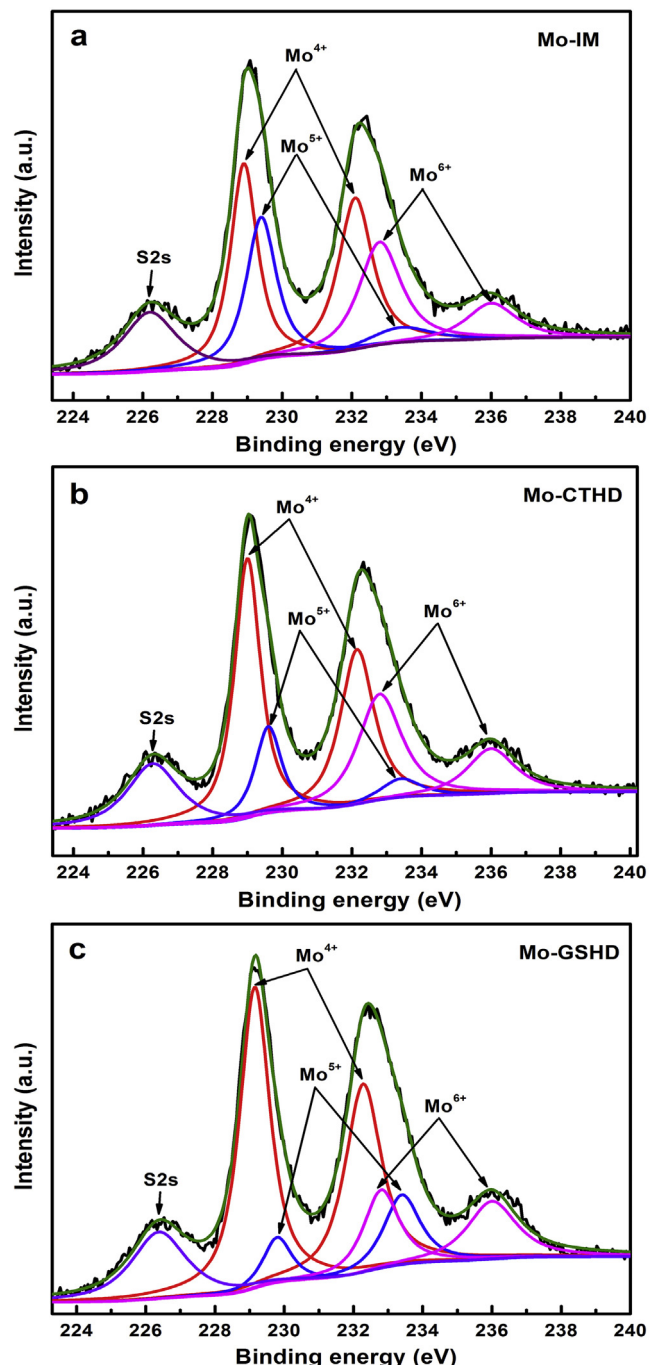


Fig. 8. Mo3d XPS patterns of sulfided Mo-IM (a), Mo-CTHD (b) and Mo-GSHD (c).

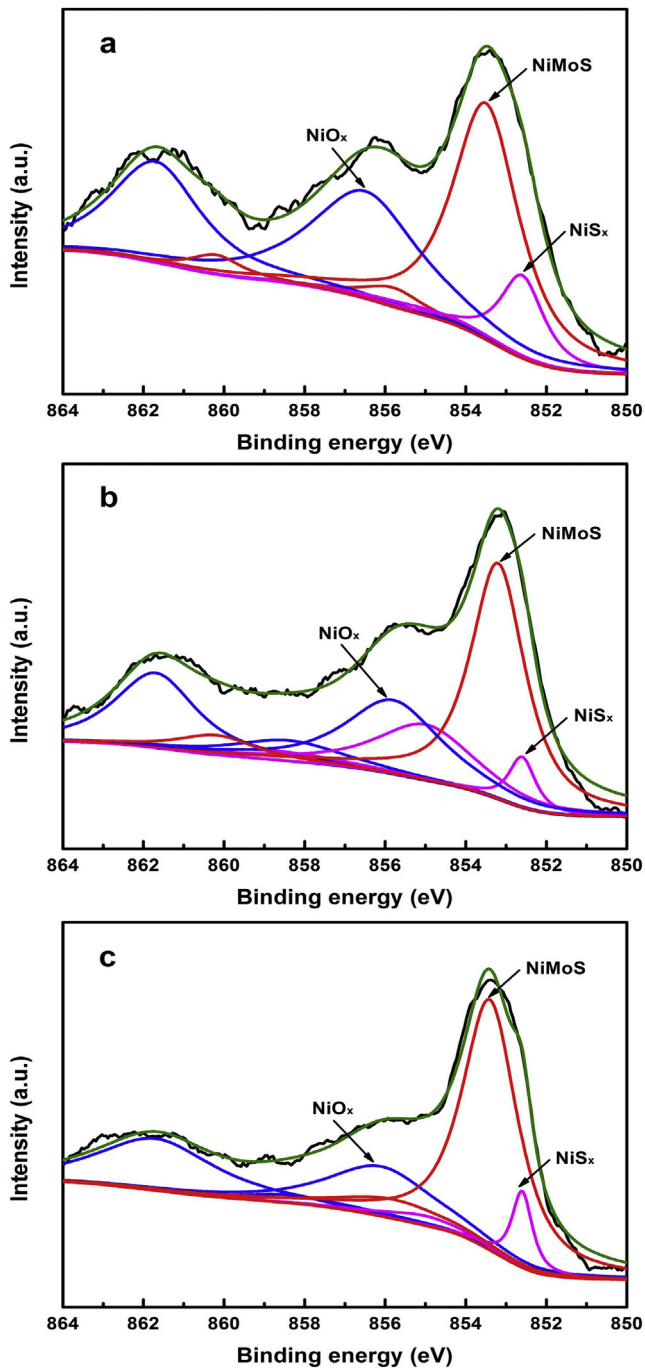


Fig. 9. Ni2p XPS patterns of sulfided NiMo-IM (a), NiMo-CTHD (b) and NiMo-GSHD (c).

3.4.2. HRTEM

HRTEM experiment of the sulfided Mo/SA catalysts was carried out to acquire more information about the morphology of the supported MoS₂ crystallites. Typical HRTEM pictures of the three sulfided catalysts are presented in Fig. 10. The black thread-like fringes in the pictures are slabs of MoS₂, as confirmed by EDS. To obtain a quantitative comparison of the stacking layer numbers and lengths of supported MoS₂ slabs, statistical analyses were performed on the basis of approximately 20 images, containing 300–500 slabs taken from different regions of each sample. Accord-

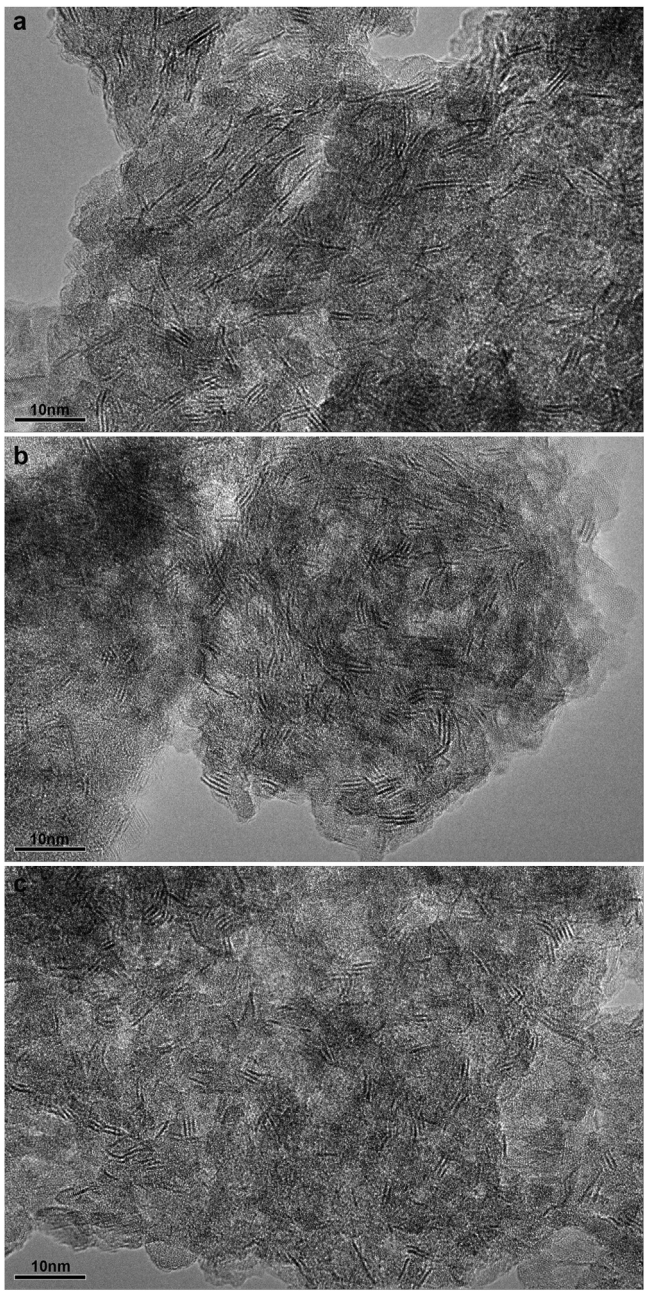


Fig. 10. HRTEM images of sulfided Mo-IM (a), Mo-CTHD (b) and Mo-GSHD (c).

ing to the literatures [56,57], the average slab length and stacking degree were expressed by the following equations:

$$\bar{L} = \frac{\sum_{i=1}^n x_i L_i}{\sum_{i=1}^n x_i} \quad \text{and} \quad \bar{N} = \frac{\sum_{i=1}^n x_i N_i}{\sum_{i=1}^n x_i} \quad (4)$$

where x_i is the number of MoS₂ slabs possessing L_i length or N_i number of layers, and L_i and N_i are the length and layer number of MoS₂ slabs in each stack, respectively.

The statistical results of the stacking layer numbers and the length distributions of the MoS₂ slabs on sulfided Mo-IM, Mo-CTHD and Mo-GSHD are shown in Fig. 11. For sulfided Mo-IM, most of the slabs are long and single-layered, while sulfided Mo-CTHD and Mo-GSHD have more short and multilayered slabs. In addition, the

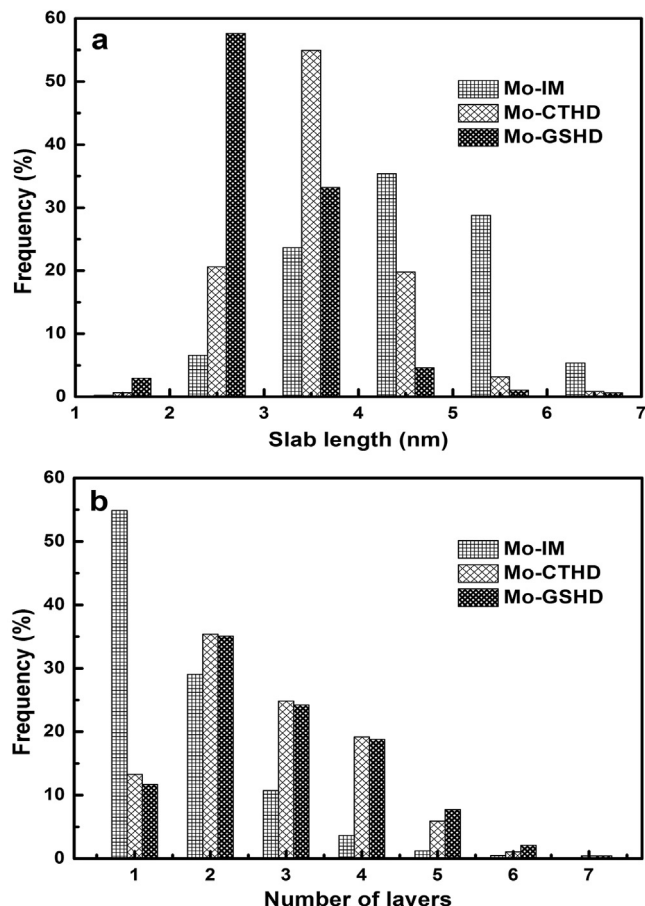


Fig. 11. Distributions of the lengths (a) and layer numbers (b) of MoS₂ slabs on sulfided Mo-IM, Mo-CTHD and Mo-GSHD.

Table 3
HRTEM statistic results on the different catalysts.

Catalyst	\bar{L} (nm)	\bar{N}	f_{Mo}
Mo-IM	4.4	1.7	0.26
Mo-CTHD	3.5	2.7	0.32
Mo-GSHD	2.8	2.8	0.37
NiMo-IM	4.0	2.0	0.27
NiMo-CTHD	3.3	2.9	0.34
NiMo-GSHD	2.7	3.0	0.40

sulfided Mo-GSHD possesses a more concentrated size distribution of MoS₂ slabs than the other two catalysts. As presented in Table 3, the average length of the MoS₂ slabs on the three catalysts increases in the order of Mo-GSHD < Mo-CTHD < Mo-IM, whereas the average stacking number of MoS₂ slabs increases in the order of Mo-IM < Mo-CTHD < Mo-GSHD, indicating that Mo-GSHD has the shortest length and the highest stacking of MoS₂ slabs among the three catalysts.

After the incorporation of Ni into Mo/SA, the average stacking layer number (\bar{N}) and slab length (\bar{L}) of MoS₂ slabs on NiMo-IM, NiMo-CTHD and NiMo-GSHD were calculated, and the results are displayed in Table 3. By comparison with the corresponding monometallic catalysts, the presence of Ni in the bimetallic catalysts reduces the MoS₂ slab length but slightly increases the MoS₂ stacking number, in accordance with the literature [48].

The results of the MoS₂ dispersion in Table 3 indicate that the MoS₂ dispersion obtained for the NiMo catalysts decreases in the order of NiMo-GSHD > NiMo-CTHD > NiMo-IM, similar to the trend for the Mo catalysts. The higher MoS₂ dispersion of Mo-CTHD and

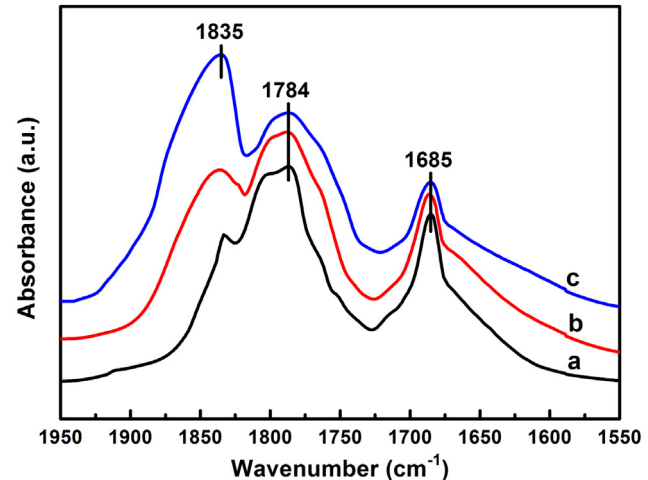


Fig. 12. IR spectra of NO adsorbed on sulfided NiMo-IM (a), NiMo-CTHD (b) and NiMo-GSHD (c).

Mo-GSHD than Mo-IM is because the reduced viscosity of aqueous solution under the hydrothermal conditions promotes the diffusion of Mo species into the support pore channels, and the remnant carbonaceous species generated from the decomposition of gemini surfactant during calcination can prevent the aggregation of molybdate oxides [58,59]. The higher MoS₂ dispersion of Mo-GSHD than Mo-CTHD originates from the better dispersing ability of gemini surfactant with larger size than CTAB. After the incorporation of Ni into Mo/SA, the high MoS₂ dispersion of Mo-GSHD facilitates the generation of more Ni-Mo-S active sites because MoS₂ slabs can serve as secondary support for nickel promoter [60,61].

The above results indicate that the Mo species on Mo-GSHD have best dispersion among the three monometallic catalysts, which originates from the transformation of the polymolybdate anions into GSMP. In GSMP, the polymolybdate anions interact with 16-N₂-16²⁺ through the charge effect, greatly promoting the dispersion of Mo precursors. The above FT-IR (Fig. 3) demonstrated the interaction between GSMP and the SA support, avoiding the strong interaction between the molybdate and the SA support. As a result, the strong Mo-support interaction is weakened, improving the stacking of the as-prepared MoS₂ and Ni-Mo-S phases.

The above analyses indicate that the Mo phases obtained by the gemini surfactant-assisted hydrothermal deposition possess high dispersion and improved stacking, facilitating the ultra-deep HDS of 4,6-DMDBT with steric hindrance.

3.4.3. NO-IR

The IR patterns of NO adsorbed on sulfided NiMo/SiO₂-Al₂O₃ catalysts are shown in Fig. 12. Three absorption bands at 1835, 1784 and 1685 cm⁻¹ are seen for the sulfided bimetallic catalysts. The band at 1835 cm⁻¹ is attributed to NO adsorbed on nickel species, and the other two bands at 1784 and 1685 cm⁻¹ are attributed to NO adsorbed on molybdenum species [62].

The peak intensity of nickel species in NiMo-GSHD is higher than NiMo-CTHD and NiMo-IM, while that of molybdenum species is lower. This can be explained as follows: since the supported MoS₂ slabs can serve as secondary support for nickel promoter [63], NiMo-GSHD with higher MoS₂ dispersion than NiMo-CTHD and NiMo-IM (Table 3) has more sites for accommodating the nickel species. Thus, the number of MoS₂ edge sites on NiMo-GSHD reduces obviously because of the Ni occupation, producing exposed and dispersed nickel sites in the Ni-Mo-S phases [64]. Therefore, NiMo-GSHD possesses more nickel sites in supported Ni-Mo-S phases and less Mo sites than the other two catalysts. In

Table 4

HDS results of 4,6-DMDBT on the different catalysts.

Catalyst	k_{HDS}^a (10^{-7} mol g $^{-1}$ s $^{-1}$)	TOF b $\times 10^4$ (s $^{-1}$)	Product selectivity c (%)				Product ratio c	
			TH + HH	MCHT	DMBCH	DMBP	(TH + HH)/MCHT	MCHT/DMBP
Mo-IM	0.32	1.72	15.6	47.1	11.9	25.4	0.33	1.85
Mo-CTHD	0.47	2.24	15.1	51.0	12.7	21.2	0.30	2.41
Mo-GSHD	0.70	2.83	14.6	54.1	13.7	17.6	0.27	3.07
NiMo-IM	3.16	5.62	9.3	58.1	4.1	28.5	0.16	2.04
NiMo-CTHD	4.18	7.34	8.5	63.6	4.6	23.3	0.13	2.72
NiMo-GSHD	5.78	9.21	7.3	68.7	5.3	18.7	0.11	3.67

^a Calculated with the 4,6-DMDBT conversion at about 30%.^b Number of the reacted 4,6-DMDBT molecules per second and per Mo atom at the edge surface.^c Determined at about 50% of the total 4,6-DMDBT conversion by changing liquid hourly space velocity.

a word, the above NO-IR results demonstrate that NiMo-GSHD has more supported Ni-Mo-S active sites than NiMo-CTHD and NiMo-IM.

3.5. Catalytic activity

4,6-DMDBT was used as feedstock to estimate the HDS activity of the prepared catalysts. 4,6-DMDBT HDS involves the following routes: hydrogenation (HYD), dealkylation, isomerization and direct desulfurization (DDS). The main detected products from 4,6-DMDBT HDS were dimethylbicyclohexyl (3,3'-DMBCH), tetrahydrodimethylbibenzothiophene (4,6-THDMDBT), 3,3'-dimethylbiphenyl (3,3'-DMBP), hexahydrodimethylbibenzothiophene (4,6-HHDMDBT) and methylcyclohexyltoluene (3,3'-MCHT). According to the analysis of the HDS products on the prepared catalysts, the routes of isomerization and dealkylation can be ignored.

The HDS rate constant k_{HDS} and TOF values of the six prepared catalysts are shown in Table 4. The k_{HDS} value on Mo-GSHD reaches 0.70×10^{-7} mol g $^{-1}$ s $^{-1}$, two times as high as that on Mo-IM and 33% higher than that on Mo-CTHD. The TOF value of Mo-GSHD is also higher than that Mo-IM and Mo-CTHD. In view of the fact that the incorporation of Ni into the monometallic molybdenum catalysts improves the HDS activity [65], the reaction rate constant and TOF of the bimetallic catalysts are displayed in Table 4. The TOF and reaction rate constant of NiMo-GSHD are higher than those of NiMo-IM and NiMo-CTHD, indicating the higher activity of NiMo-GSHD than the other two bimetallic catalysts.

The reaction product distributions of the six catalysts at the same 4,6-DMDBT conversion (50%) were compared, and the results are presented in Table 4. The ratios of 3,3'-MCHT to 3,3'-DMBP for all catalysts are higher than one, indicating that the HYD route is preferred to the DDS route because of the steric hindrance effect of 4,6-DMDBT. The 3,3'-MCHT/3,3'-DMBP ratio of Mo-GSHD is higher than the other two monometallic catalysts, indicating better HDS selectivity of Mo-GSHD for the HYD route. Moreover, the selectivities for 4,6-HHDMDBT, 4,6-THDMDBT and the (4,6-HHDMDBT + 4,6-THDMDBT)/3,3'-MCHT ratio on Mo-GSHD are lower than those on Mo-IM and Mo-CTHD, indicating the higher hydrogenolysis desulfurization ability of Mo-GSHD. The un-promoted Mo catalysts are efficient for the hydrogenation reaction of 4,6-DMDBT; however, they are unable to efficiently removing sulfur from the hydrogenated intermediates. Incorporation of Ni into the Mo/SA catalysts results in an improvement of the 3,3'-MCHT/3,3'-DMBP ratio, indicating the enhancement effect of Ni on the HDS selectivity for the HYD route. Meanwhile, incorporating Ni into the Mo/SA catalysts leads to a decrease in the (4,6-HHDMDBT + 4,6-THDMDBT)/3,3'-MCHT ratio, showing that nickel improves the rate of sulfur removal from the hydrogenated intermediates (4,6-HHDMDBT and 4,6-THDMDBT) of the HYD route. In addition, NiMo-GSHD has higher 3,3'-MCHT selectivity and 3,3'-MCHT/3,3'-DMBP ratio than NiMo-IM and NiMo-CTHD, indicating

Table 5
FCC diesel HDS results on the three bimetallic catalysts.

Catalyst	Total sulfur content in feedstock ($\mu\text{g g}^{-1}$)	Total sulfur content in product ($\mu\text{g g}^{-1}$)	HDS ratio (%)
NiMo-IM	3920	239.1	93.9
NiMo-CTHD	3920	113.7	97.1
NiMo-GHD	3920	27.4	99.3

its better HYD selectivity. The supported MoS₂ slabs can serve as secondary support for nickel species [60,66]; therefore, NiMo-GSHD, with the superior MoS₂ dispersion, provides sufficient MoS₂ sites to accommodate the Ni species. As a result, more Ni-Mo-S active sites are formed on NiMo-GSHD than NiMo-IM and NiMo-CTHD (Fig. 12), enhancing the HDS activity of NiMo-GSHD.

The stability results about the 4,6-DMDBT and FCC diesel HDS performances of the three bimetallic catalysts (Fig. S3) show that the total sulfur contents in the 4,6-DMDBT and FCC diesel HDS products over the three bimetallic catalysts remain stable during the operation, demonstrating good stability of the three bimetallic catalysts. From Table 5, NiMo-GSHD produces the highest HDS ratio and the lowest sulfur content in product among the three bimetallic catalysts, showing its advantage in the ultra-deep HDS of FCC diesel.

The HDS reaction results of 4,6-DMDBT and FCC diesel indicate that NiMo-GSHD possesses higher HDS activity than the other two bimetallic catalysts. For understanding their different activities, the HDS activities of the bimetallic catalysts were correlated with the structures of their metal phases. In the Ni-Mo-S phases supported on alumina, the brim sites (the bottom and top layers of Ni-Mo-S phases) have HYD activity and the edge sites have DDS activity [67]. Compared with NiMo-IM and NiMo-CTHD, NiMo-GSHD has a higher MoS₂ dispersion (0.40) and a superior average stacking number (3.0) (Table 3), generating more Ni-Mo-S active sites with sufficient brim sites; therefore, the prehydrogenation activity of NiMo-GSHD for 4,6-DMDBT with steric hindrance is markedly improved (Fig. 13). The prehydrogenated products (4,6-THDMDBT and 4,6-HHDMDBT) without steric hindrance are much easier to be desulfurization via hydrogenolysis on the edge sites of Ni-Mo-S phases than initial 4,6-DMDBT. Therefore, NiMo-GSHD, with more edge sites due to its better metal dispersion, possesses higher 3,3'-MCHT selectivity than NiMo-IM and NiMo-CTHD.

Compared with NiMo-IM and NiMo-CTHD, NiMo-GSHD has smaller metal nanoparticles evidenced by XRD and STEM characterizations, higher Mo sulfidation evidenced by XPS characterization, higher dispersion of supported MoS₂ with good stacking evidenced by HRTEM characterization, and more NiMoS active phases evidenced by NO-IR characterization than NiMo-IM and NiMo-CTHD, endowing itself with superior catalytic performance for the HDS of 4,6-DMDBT and FCC diesel.

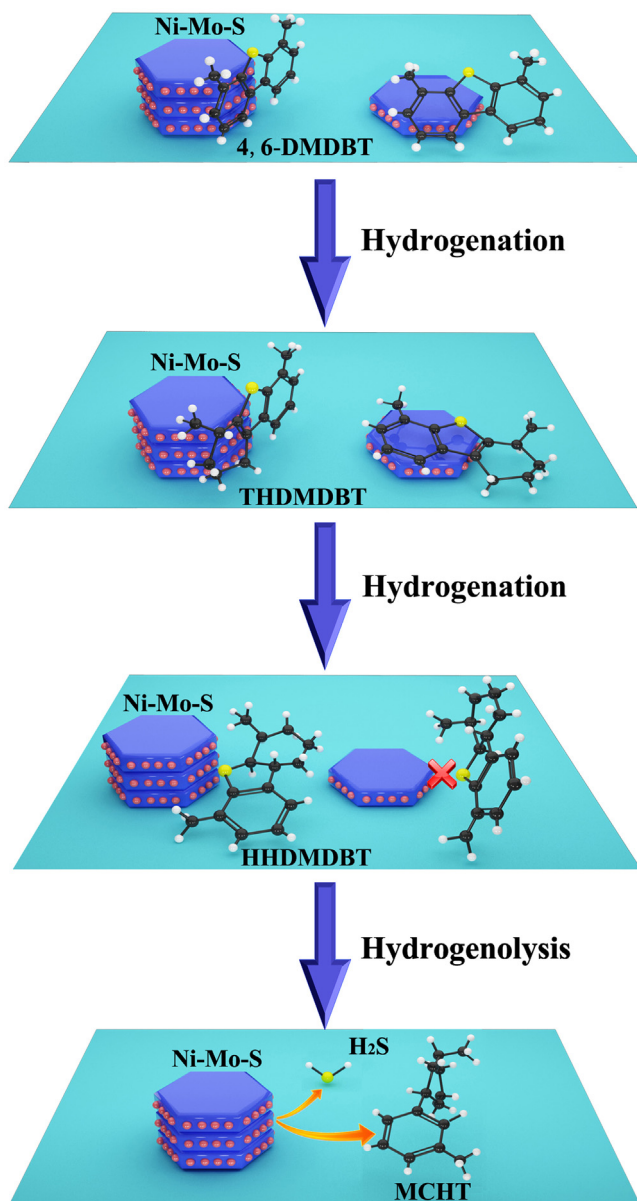


Fig. 13. Schematic diagram for eliminating steric hindrance of 4,6-DMDBT through the HYD route on sulfided NiMo-GSHD with the high dispersion and superior stacking of Ni-Mo-S phases.

4. Conclusions

The $\text{SiO}_2\text{-Al}_2\text{O}_3$ -supported Mo and NiMo HDS catalysts were developed on the basis of gemini surfactant-dispersed Mo precursor. The traditional Mo species used to prepare HDS catalysts have been converted into novel gemini surfactant-linked $\text{Mo}_{8}\text{O}_{26}^{4-}$ precursor (GSMP), promoting the dispersion of Mo species. The interaction between GSMP and the $\text{SiO}_2\text{-Al}_2\text{O}_3$ support avoids the strong Mo-support interaction, improving the stacking of MoS_2 and Ni-Mo-S phases. The as-prepared Ni-Mo-S phases on the $\text{SiO}_2\text{-Al}_2\text{O}_3$ support possess superior metal morphology with high dispersion and improved stacking, providing a large number of accessible Ni-Mo-S active sites. The corresponding catalyst presents higher activity for the hydrogenation and direct desulfurization of sterically hindered 4,6-dimethyldibenzothiophene (4,6-DMDBT) than its counterparts prepared via impregnation and the cetyltrimethylammonium bromide-assisted hydrothermal

method. This method finely adjusts the morphology of supported Ni-Mo-S phases in HDS catalysts for the ultra-deep HDS of fuel.

Acknowledgment

The authors gratefully acknowledge the financial support of the National Natural Science Foundation of China (Grant Nos. 21076228 and U1162116).

Appendix A. Supplementary data

Supplementary data associated with this article can be found, in the online version, at <http://dx.doi.org/10.1016/j.apcatb.2016.10.078>.

References

- [1] C. Song, X. Ma, *Appl. Catal. B: Environ.* 41 (2003) 207–238.
- [2] F. Bataille, J.L. Lemberton, G. Pérot, P. Leyrit, T. Cseri, N. Marchal, S. Kasztelan, *Appl. Catal. A: Gen.* 220 (2001) 191–205.
- [3] A. Stanislaus, A. Marafi, M.S. Rana, *Catal. Today* 153 (2010) 1–68.
- [4] P.T. Vasudevan, J.L.G. Fierro, *Cat. Rev.* 38 (1996) 161–188.
- [5] H. Topsøe, B.S. Clausen, *Cat. Rev.* 26 (1984) 395–420.
- [6] T. Hayden, J. Dumesic, R. Sherwood, R. Baker, *J. Catal.* 105 (1987) 299–318.
- [7] R. Prins, V.H.J. De Beer, G.A. Somorjai, *Cat. Rev.* 31 (1989) 1–41.
- [8] E.J.M. Hensen, V.H.J. de Beer, J.A.R. van Veen, R.A. van Santen, *Catal. Lett.* 84 (2002) 59–67.
- [9] A. Gutiérrez-Alejandre, G. Llaurrabaquio-Rosas, J. Ramírez, G. Busca, *Appl. Catal. B: Environ.* 166–167 (2015) 560–567.
- [10] N. Rinaldi, K. Al-Dalama, T. Kubota, Y. Okamoto, *Catal. A: Gen.* 360 (2009) 130–136.
- [11] S. Tauster, S. Fung, R. Baker, J. Horsley, *Science* 211 (1981) 1121–1125.
- [12] Y. Okamoto, T. Imanaka, *J. Chem. Phys.* 92 (1988) 7102–7112.
- [13] Y. Chen, L. Zhang, *Catal. Lett.* 12 (1992) 51–62.
- [14] L. Lizama, T. Klimova, *Appl. Catal. B: Environ.* 82 (2008) 139–150.
- [15] D. Valencia, T. Klimova, *Catal. Today* 166 (2011) 91–101.
- [16] H. Wu, A. Duan, Z. Zhao, D. Qi, J. Li, B. Liu, G. Jiang, J. Liu, Y. Wei, X. Zhang, *Fuel* 130 (2014) 203–210.
- [17] A. Wang, Y. Wang, T. Kabe, Y. Chen, A. Ishihara, W. Qian, *J. Catal.* 199 (2001) 19–29.
- [18] T. Klimova, M. Calderón, J. Ramírez, *Appl. Catal. A: Gen.* 240 (2003) 29–40.
- [19] F. Sánchez-Minero, J. Ramírez, A. Gutiérrez-Alejandre, C. Fernández-Vargas, P. Torres-Mancera, R. Cuevas-García, *Catal. Today* 133–135 (2008) 267–276.
- [20] S. Hwang, J. Lee, S. Park, D.R. Park, J.C. Jung, S.B. Lee, I.K. Song, *Catal. Lett.* 129 (2009) 163–169.
- [21] D.P. Debecker, B. Schimmoeller, M. Stoyanova, C. Poleunis, P. Bertrand, U. Rodemerck, E.M. Gaigneaux, *J. Catal.* 277 (2011) 154–163.
- [22] F.Y.A. El Kady, M.G. Abd El Wahed, S. Shaban, A.O. Abo El Naga, *Fuel* 89 (2010) 3193–3206.
- [23] J. Vakros, A. Lycourghiotis, G. Voyatzis, A. Siokou, C. Kordulis, *Appl. Catal. B: Environ.* 96 (2010) 496–507.
- [24] M.V. Landau, L. Vradman, M. Herskowitz, Y. Koltypin, A. Gedanken, *J. Catal.* 201 (2001) 22–36.
- [25] J.J. Lee, H. Kim, S.H. Moon, *Appl. Catal. B: Environ.* 41 (2003) 171–180.
- [26] J.A. Bergwerff, T. Visser, G. Leliveld, B.D. Rossenaar, K.P. de Jong, B.M. Weckhuysen, *J. Am. Chem. Soc.* 126 (2004) 14548–14556.
- [27] K.A. Leonova, O.V. Klimov, E.Y. Gerasimov, P.P. Dik, V.Y. Pereyma, S.V. Budukva, A.S. Noskov, *Adsorption* 19 (2013) 723–731.
- [28] P. Nikul'shin, A. Mozhaev, A. Pimerzin, N. Tomina, V. Konovalov, V. Kogan, *Kinet. Catal.* 52 (2011) 862–875.
- [29] Y. Fan, X. Bao, H. Wang, C. Chen, G. Shi, *J. Catal.* 245 (2007) 477–481.
- [30] K. Na, C. Jo, J. Kim, K. Cho, J. Jung, Y. Seo, R.J. Messinger, B.F. Chmelka, R. Ryoo, *Science* 333 (2011) 328–332.
- [31] R. Zana, M. Benraou, R. Rueff, *Langmuir* 7 (1991) 1072–1075.
- [32] X. Gao, I.E. Wachs, *J. Chem. Phys. B* 104 (2000) 1261–1268.
- [33] Q. Gao, T.N.K. Ofori, S.G. Ma, V.G. Komvokis, C.T. Williams, K. Segawa, *Catal. Today* 164 (2011) 538–543.
- [34] A.M. Venezia, *Catal. Today* 77 (2003) 359–370.
- [35] T.K.T. Ninh, L. Massin, D. Laurenti, M. Vrinat, *Appl. Catal. A: Gen.* 407 (2011) 29–39.
- [36] S. Texier, G. Berhault, G. Pérot, V. Harlé, F. Diehl, *J. Catal.* 223 (2004) 404–418.
- [37] T.E. Klimova, D. Valencia, J.A. Mendoza-Nieto, P. Hernández-Hipólito, *J. Catal.* 304 (2013) 29–46.
- [38] P.A. Nikulshin, V.A. Salnikov, A.V. Mozhaev, P.P. Minaev, V.M. Kogan, A.A. Pimerzin, *J. Catal.* 309 (2014) 386–396.
- [39] A.A. Pimerzin, P. Nikulshin, A. Mozhaev, A. Pimerzin, A. Lyashenko, *Appl. Catal. B: Environ.* 168 (2015) 396–407.
- [40] G. Mestl, T.K.K. Srinivasan, *Cat. Rev.* 40 (1998) 451–570.
- [41] T. Ito, K. Sawada, T. Yamase, *Chem. Lett.* 32 (2003) 938–939.
- [42] P.J. Hagrman, D. Hagrman, J. Zubietta, *Angew. Chem. Int. Ed.* 38 (1999) 2638–2684.

[43] T. He, J. Yao, *Prog. Mater. Sci.* 51 (2006) 810–879.

[44] J. Broekhoff, J. De Boer, *J. Catal.* 10 (1968) 153–165.

[45] W. Han, P. Yuan, Y. Fan, G. Shi, H. Liu, D. Bai, X. Bao, *J. Mater. Chem.* 22 (2012) 25340–25353.

[46] O.Y. Gutiérrez, F. Pérez, G.A. Fuentes, X. Bokhimi, T. Klimova, *Catal. Today* 130 (2008) 292–301.

[47] G. Li, L. Hu, J.M. Hill, *Appl. Catal. A: Gen.* 301 (2006) 16–24.

[48] O.Y. Gutiérrez, T. Klimova, *J. Catal.* 281 (2011) 50–62.

[49] R.S. Weber, *J. Catal.* 151 (1995) 470–474.

[50] J.L. Brito, J. Laine, *J. Catal.* 139 (1993) 540–550.

[51] L. Qu, W. Zhang, P.J. Kooyman, R. Prins, *J. Catal.* 215 (2003) 7–13.

[52] M.A. Domínguez-Crespo, E.M. Arce-Estrada, A.M. Torres-Huerta, L. Díaz-García, M.T. Cortez de la Paz, *Mater. Charact.* 58 (2007) 864–873.

[53] R.L. Cordero, F.G. Llambias, A.L. Agudo, *Appl. Catal.* 74 (1991) 125–136.

[54] P.A. Nikulshin, A. Mozhaev, K. Maslakov, A. Pimerzin, V. Kogan, *Appl. Catal. B: Environ.* 158 (2014) 161–174.

[55] Y. Fan, H. Xiao, G. Shi, H. Liu, Y. Qian, T. Wang, G. Gong, X. Bao, *J. Catal.* 279 (2011) 27–35.

[56] E.J.M. Hensen, P.J. Kooyman, Y. van der Meer, A.M. van der Kraan, V.H.J. de Beer, J.A.R. van Veen, R.A. van Santen, *J. Catal.* 199 (2001) 224–235.

[57] R. Singh, D. Kunzru, S. Sivakumar, *Appl. Catal. B: Environ.* 185 (2016) 163–173.

[58] P. Afanasiev, G.F. Xia, G. Berhault, B. Jouquet, M. Lacroix, *Chem. Mater.* 11 (1999) 3216–3219.

[59] D. Genuit, P. Afanasiev, M. Vrinat, *J. Catal.* 235 (2005) 302–317.

[60] T. Shimizu, K. Hiroshima, T. Honma, T. Mochizuki, M. Yamada, *Catal. Today* 45 (1998) 271–276.

[61] Y. Okamoto, K. Ochiai, M. Kawano, T. Kubota, *J. Catal.* 222 (2004) 143–151.

[62] N.-Y. Topsøe, H. Topsøe, *J. Catal.* 84 (1983) 386–401.

[63] S. Louwers, R. Prins, *J. Catal.* 133 (1992) 94–111.

[64] N. Koizumi, S. Jung, Y. Hamabe, H. Suzuki, M. Yamada, *Catal. Lett.* 135 (2010) 175–181.

[65] H. Topsøe, B.S. Clausen, N.Y. Topsøe, E. Pedersen, *Ind. Eng. Chem. Fundam.* 25 (1986) 25–36.

[66] C.K. Groot, V.H. De Beer, R. Prins, M. Stolarski, W.S. Niedzwiedz, *Ind. Eng. Chem. Prod. Res. Dev.* 25 (1986) 522–530.

[67] M. Daage, R.R. Chianelli, *J. Catal.* 149 (1994) 414–427.